

REPORT DOCUMENTATION PAGE

Form Approved
OMB No. 0704-0188

Public reporting burden for this collection of information is estimated to average 1 hour per response, including the time for reviewing instructions, searching existing data sources, gathering and maintaining the data needed, and completing and reviewing the collection of information. Send comments regarding this burden estimate or any other aspect of this collection of information, including suggestions for reducing this burden, to Washington Headquarters Services, Directorate for Information Operations and Reports, 1215 Jefferson Davis Highway, Suite 1204, Arlington, VA 22202-4302, and to the Office of Management and Budget, Paperwork Reduction Project (0704-0188), Washington, DC 20503.

| | | | | | |
|---|--|---|--|---|--|
| 1. AGENCY USE ONLY (Leave blank) | | 2. REPORT DATE | | 3. REPORT TYPE AND DATES COVERED FINAL REPORT - 01 Sep 94 - 31 Aug 9 | |
| 4. TITLE AND SUBTITLE Stable High Power Harmonic Gyro-Amplifier | | | | 5. FUNDING NUMBERS 61102/F 2301/ES | |
| 6. AUTHOR(S) Professor Luhmann, Jr | | | | | |
| 7. PERFORMING ORGANIZATION NAME(S) AND ADDRESS(ES) College of Engineering Univ of California, Davis Davis, CA 95616 | | | | 8. PERFORMING ORGANIZATION REPORT NUMBER AFOSR-TR- 96-0005 | |
| 9. SPONSORING / MONITORING AGENCY NAME(S) AND ADDRESS(ES) AFOSR/NE 110 Duncan Avenue Suite B115 Bolling AFB DC 20332-0001 | | | | 10. SPONSORING / MONITORING AGENCY REPORT NUMBER F49620-94-1-0426 | |
| 11. SUPPLEMENTARY NOTES | | | | | |
| 12a. DISTRIBUTION / AVAILABILITY STATEMENT APPROVED FOR PUBLIC RELEASE: DISTRIBUTION UNLIMITED | | | | 12b. DISTRIBUTION CODE | |
| 13. ABSTRACT (Maximum 200 words) Our second-harmonic smooth-bore gyro-TWT, which generated a record-breaking 207 kW and was stable without rf input, was found to be in good agreement with our large-signal simulation code for an axial velocity spread of 14% and therefore improvement is anticipated through optimization of the MIG electron gun. an analytical theory of slotted harmonic gyro-TWT amplifiers, which can be used to evaluate stability, has been described in a paper submitted for publication to the IEEE Trans. on Plasma Science's Special Issue on High Power Microwave Generation. A new mode-selective interaction circuit has been fabricated for the slotted gyro-TWT to improve its stability by employment of the slicing technique successful employed in our second-harmonic smooth-bore gyro-TWT. | | | | | |
| 14. SUBJECT TERMS | | | | 15. NUMBER OF PAGES | |
| | | | | 16. PRICE CODE | |
| 17. SECURITY CLASSIFICATION OF REPORT UNCLASSIFIED | | 18. SECURITY CLASSIFICATION OF THIS PAGE UNCLASSIFIED | | 19. SECURITY CLASSIFICATION OF ABSTRACT UNCLASSIFIED | |
| 20. LIMITATION OF ABSTRACT | | | | | |

19960129 135

Stable High Power Harmonic Gyro-Amplifier

Final Report: 10/20/95

AFOSR-Tri-Service Grant No. F49620-94-1-⁰⁴²⁶0396

Principal Investigator: N.C. Luhmann, Jr.

Stable High-Power Harmonic Gyro-Amplifiers

Table of Contents

- 1. Bullet Summary**
- 2. Research Progress during 9/1/94 -- 8/31/95**
 - 2.1 Summary**
 - 2.2 High Power s^{th} -Harmonic TE_{s1} Gyro-TWT Amplifiers**
 - 2.2.1 Second-Harmonic TE_{21} Gyro-TWT Experiment**
 - 2.2.1.1 Analysis**
 - 2.2.1.2 $\text{TE}_{21}/\text{TE}_{11}$ Mode Converter**
 - 2.2.1.3 Mode-Selective Circuit**
 - 2.3 Slotted High-Harmonic Gyro-TWT Amplifiers**
 - 2.3.1 Linear Stability Theory**
 - 2.3.2 Third-Harmonic Slotted Gyro-TWT Experiment**
 - 2.3.2. Small-Signal Experimental Results**
 - 2.3.2.2 Large-Signal Test Preparation**
 - 2.4 Third-Harmonic Gyrotron Reflection Amplifier**
 - 2.4.1 $\text{TE}_{31}^{(3)}$ Gyrotron Reflection Amplifier with a Cusp Gun**
 - 2.4.2 $\text{TE}_{41}^{(3)}$ Gyrotron Reflection Amplifier with a MIG Gun**
- 3. References**
- 4. Figures and Tables**
- 5. Publications and Conference Presentations during 9/1/94 -- 8/31/95**
- 6. UCLA Subcontract Annual Progress Report**

1. Bullet Summary

- Our second-harmonic smooth-bore gyro-TWT, which generated a record-breaking 207 kW and was stable without rf input, was found to be in good agreement with our large-signal simulation code for an axial velocity spread of 14% and therefore improvement is anticipated through optimization of the MIG electron gun.
- The gain of our second-harmonic smooth-bore TE_{21} gyro-TWT was found in simulation to increase if the stability can be enhanced by adding loss to the circuit.
- A longer TE_{21}/TE_{11} mode converter with a much smaller center-frequency shift and a bandwidth of 4% has been designed for the second-harmonic TE_{21} gyro-TWT.
- An analytical theory of slotted harmonic gyro-TWT amplifiers, which can be used to evaluate stability, has been described in a paper submitted for publication to the IEEE Trans. on Plasma Science's Special Issue on High Power Microwave Generation.
- A more stable 30 kW slotted third-harmonic gyro-TWT was designed for Varian as their ARPA-funded 95 GHz fast-wave amplifier.
- The large-signal hot-tests of the slotted third-harmonic gyro-TWT, which was previously tested in the small-signal regime by using axis-encircling electron beams produced by our gyroresonant rf accelerator and found to be stable, can now be performed since we have improved the efficiency of our input coupler.
- A new mode-selective interaction circuit has been fabricated for the slotted gyro-TWT to improve its stability by employment of the slicing technique successfully employed in our second-harmonic smooth-bore gyro-TWT.
- A lightweight third-harmonic gyrotron reflection amplifier using a permanent magnet and a modest voltage of 50 kV has been designed that is capable of generating 25 kW CW at 35 GHz with an efficiency of 45%.

2. Research Progress during 9/1/94 -- 8/31/95

2.1 Summary

The focus of our Tri-Service University Research Program in Vacuum Electronics has continued to be on basic research issues associated with operating harmonic gyrotron devices as high-power, coherent millimeter-wave amplifiers. Substantial theoretical and experimental progress has been achieved. We analysed our recent second-harmonic gyro-TWT amplifier experiment with our large-signal gyro-TWT code and obtained excellent agreement with our experimental results. We learned that the axial velocity spread of the electron beam was 14%, which is significantly higher than the predictions of 8% from the EGUN code. Although the stable second-harmonic gyro-TWT generated an output power of 207 kW, which exceeded the highest previous gyro-TWT power level of 120 kW, it can be further increased to 400 kW by modifying the MIG electron gun to reduce the velocity spread to the design value. We learned that the performance of the amplifier can also be improved by adding some loss to the circuit to further improve its stability. At the higher levels of output power, it will be necessary to replace the output coupler by a transducer more resistant to high power breakdown. A new TE_{21}/TE_{11} mode converter has been designed for the second-harmonic TE_{21} gyro-TWT which is predicted to yield a bandwidth of 4%.

As another part of this grant's research, we designed a third-harmonic gyro-TWT amplifier for Varian as their 95 GHz fast-wave amplifier in their ARPA-funded development program. A stability theory of slotted harmonic gyro-TWT amplifiers, has been developed and described in a paper submitted for publication. Employing this theory, we discovered that the initial Varian design was unstable to a peniotron mode and then modified the electron beam parameters to suppress the peniotron mode. The new design is predicted to yield 30 kW with 20% efficiency and a gain of 40 dB. We have also continued our hot-tests of a lower frequency scaled model by using the axis-encircling electron beams produced by a gyroresonant rf accelerator. The scaled single-section amplifier verified the stability of the design and yielded a small-signal gain of 13 dB with 3% bandwidth. Unfortunately, the experiments could not test the large-signal properties of the amplifier because the input coupler was too inefficient to drive the system into saturation. We are currently prepared to perform the large-signal hot-tests of the slotted third-harmonic gyro-TWT now that we have improved the efficiency of our input coupler. To improve its stability, the previous interaction circuit has been replaced by a new mode-selective interaction circuit that has been sliced, a technique that was successfully employed in our second-harmonic smooth-bore gyro-TWT.

In addition, we have utilized the basic principle that any rf oscillator can be employed as a reflection amplifier to design a lightweight 35 GHz gyrotron amplifier. A reflection amplifier

yields its highest gain when it is operated just under the start-oscillation condition. High efficiency is predicted for the 50 kV, third-harmonic gyrotron. Operation at the third harmonic allows the required magnetic field for 35 GHz generation to be supplied by a 4.5 kG permanent magnet. Two gyrotrons employing sliced circuits for mode control have been evaluated with a nonlinear code and found to be capable of producing a CW output power of 25 kW. A third-harmonic TE₄₁ gyrotron utilizing a magnetron injection electron gun is predicted to yield 46% device efficiency with a single-stage depressed collector and 17% without one, while a more ideal axis-encircling electron beam from a Cusp electron gun can drive a third-harmonic TE₃₁ gyrotron with a device efficiency of 23%, which can be increased to 45% through the use of a depressed collector.

Although we are working with Varian to use our slotted third-harmonic gyro-TWT design to develop a high-average-power, 95 GHz fast-wave amplifier for ARPA, the information on this work is also being actively disseminated to the microwave community to aid other companies and laboratories in the design of high power, high frequency fast-wave amplifiers. For example, we have offered to make available our rf accelerated electron beam source to test concepts developed by the various ARPA funded groups, including Northrop, NRL and Litton, in addition to Varian.

2.2 High Power s^{th} -Harmonic TE _{s 1} Gyro-TWT Amplifiers

The superb characteristics of the s^{th} -harmonic TE _{s 1} gyro-TWT amplifier are due to three key features. The first is that there can be no competing first harmonic emission [1]. If a gyro-TWT is designed so that the electrons are in resonance at the s^{th} -harmonic with a cylindrical waveguide's TE _{s 1} mode, then there are no modes which can be excited at the fundamental frequency, as can be seen in Fig. 1 for the case of a second-harmonic TE₂₁ gyro-TWT. The second feature is that the allowable electron beam current for stability and therefore the output power is much higher [2] than at the fundamental frequency due to the weaker strength of the harmonic interactions, which leads to high power operation. Figure 2 shows that the critical beam current for the absolute instability in an s^{th} -harmonic TE _{s 1} gyro-TWT increases strongly with the harmonic number. The third feature is that the required magnetic field can be reduced by a factor of s in a TE _{s 1} gyro-TWT, which often allows conventional electromagnets or permanent magnets to be used for millimeter-wave generation rather than more troublesome superconducting systems.

2.2.1 Second-Harmonic TE₂₁ Gyro-TWT Experiment

A recent theory [2] for achieving stability in high power gyrotron traveling wave (gyro-TWT) amplifiers has been verified in our second-harmonic TE₂₁ gyro-TWT experiment and was reported in the paper, "Demonstration of Marginal Stability Theory by a 200 kW Second-Harmonic Gyro-TWT Amplifier," by Q.S. Wang, D.B. McDermott and N.C. Luhmann, Jr., which was

accepted for publication by the *Physics Review Letters*. A more complete description of this experiment was presented in the paper, "Operation of a Stable 200 kW Second-Harmonic Gyro-TWT Amplifier," by Q. S. Wang, D. B. McDermott and N. C. Luhmann, Jr., which was submitted to the *IEEE Trans. on Plasma Science's Special Issue on High Power Microwave Generation*. By keeping the interaction length shorter than the critical oscillation length for the competing modes, stability was achieved. The experiment also verified the theoretical prediction that harmonic gyro-TWT's can produce higher power because their weaker interaction yields a higher threshold electron current for oscillation. The second-harmonic gyro-TWT amplifier stably generated 207 kW, nearly twice the level achieved by fundamental-harmonic gyro-TWT's.

2.2.1.1 Analysis

A nonlinear self-consistent code [3] was used to simulate the amplifier's performance to determine the beam's axial velocity spread. The simulation results for an 80 kV, 20 A, $v_{\perp}/v_{\parallel} = 1.1$ beam with $r_c/r_w = 0.4$ and an axial velocity spread of 14% in a magnetic field of $B_0 = 0.97 B_g$ have been included with the experimental bandwidth in Fig. 3. The theory agrees quite well with the experimental results. For these values, the predicted small-signal gain of 21.5 dB at 15.7 GHz is also in good agreement with the experimental value of 22 dB. The device can be significantly enhanced by reducing the electron beam's axial velocity spread. As shown in Fig. 4, the amplifier is predicted to generate 400 kW with an efficiency of 20% for an axial velocity spread of 8%. It is evident that the relatively high velocity spread has limited the output power level as well as the bandwidth. The device can also be improved by adding some loss to the circuit to further strengthen the amplifier's stability. An output power of 500 kW is predicted for a 25 A electron beam as shown in Fig. 5. Higher gain can also result in a more stable device. A more stable amplifier would allow a wider magnetic field operating range. By increasing the magnetic field from $B/B_g = 0.97$ to 0.98, a gain of 30 dB would result (see Fig. 4).

2.2.1.2 TE₂₁/TE₁₁ Mode Converter

Although our high power second-harmonic gyro-TWT amplifier did not show any signs of microwave breakdown, as the power is increased, eventually the overmoded amplifier will breakdown in the output coupler's fundamental-mode rectangular waveguide. By replacing the output coupler by an overmoded beat-wave mode converter [4], the threshold breakdown level can be increased into the megawatt range. Broadband linearly-polarized beat-wave mode converters have been developed and tested [5] by our group to transform the high-order cylindrical TE_{m1} output wave from harmonic gyrotron amplifiers into the more useful TE₁₁ fundamental waveguide mode. Our research on these mode converters was summarized in the paper, "Broadband

Linearly-Polarized Beat-Wave TE_{m1}/TE_{11} Mode Converter," by D.B. McDermott, J. Pretterebner, C.K. Chong, C.F. Kinney, M.M. Razeghi, and D.B. McDermott, which will be published by the *IEEE Trans. on Microwave Theory and Tech.* in January, 1996. The converter's corrugation period is equal to the beat between the two waves and the bandwidth is predicted to be inversely proportional to the number of periods. Four-period TE_{31}/TE_{11} and TE_{41}/TE_{11} converters with an azimuthal perturbation of $m_c=4$ and $m_c=5$, respectively, have yielded a peak conversion efficiency of 98% with a bandwidth greater than 3%. However, it has been observed in measurements that the strong coupling in a short converter can lead to a shift of the center-frequency with an accompanying reduction of the efficiency and bandwidth. A two-period TE_{41}/TE_{11} converter with 5% bandwidth displayed a 5% frequency shift and a conversion efficiency of only 86%.

An $m_c = 3$ beat-wave TE_{21}/TE_{11} mode converter has been designed for the TE_{21} gyro-TWT amplifier with four periods as in our successful, 98% efficient, TE_{31}/TE_{11} and TE_{41}/TE_{11} converters that displayed only a slight shift of their center frequencies. Figure 6 shows a schematic of the the new converter and its predicted bandwidth of 4% is shown in Fig. 7.

2.2.1.3 Mode-Selective Circuit

To ensure the stability of the amplifier, the circular interaction waveguide was sliced [6] axially with two cuts separated in azimuth by 90° as shown in Fig. 8. In such an arrangement, the wall currents supporting the TE_{mn} modes with odd m are interrupted, while the operating TE_{21} mode remains unperturbed. When the most threatening $TE_{11}^{(2)}$ and $TE_{31}^{(3)}$ gyrotron backward-wave oscillation (gyro-BWO) modes [7] are suppressed, a much longer interaction length (limited by the critical length for the $TE_{41}^{(4)}$ gyro-BWO mode) can then be used to boost the amplifier gain. The interaction section for the $TE_{21}^{(2)}$ gyro-TWT amplifier experiment was chosen to be 80% of the critical length for the $TE_{41}^{(4)}$ mode.

The mode-selective sliced circuit performed as anticipated. For optimum suppression of the odd- m TE_{mn} modes, the sliced interaction waveguide was surrounded by a lossy dielectric (teflon) cylinder coated with graphite to absorb the waves leaking through the slices. Excluding the input and output coupling losses, the insertion loss for the operating TE_{21} mode through the entire sliced amplifier system was measured to be below 1.5 dB over the frequency bandwidth of interest, whereas the insertion loss for the TE_{11} mode at the most likely oscillating frequency was measured to exceed 24 dB. The TE_{11} mode was launched in the cold tests by a rectangular to circular waveguide transition. Although the insertion loss of the TE_{31} mode was not measured due to the unavailability of an appropriate transducer, its suppression is expected to be similar to that of the TE_{11} mode because of their similarity in mode symmetry.

In addition to super-power amplifiers, other applications exist for the sliced mode-selective circuit used in the second-harmonic gyro-TWT. For example, the mode-selective circuit can be used to suppress the beam breakup instability in high current linear rf accelerators. The beam breakup is due to the growth of TE_{n1} modes. The TE_{11} dipole interaction is the strongest, but the TE_{21} quadrupole has also been observed to grow if the beam current is sufficiently high. The sliced circuit with its 30 dB/m of attenuation is appropriate for suppressing all TE_{n1} modes, while leaving the linac's operating TM_{01} mode unaffected. A circuit with six cuts separated in azimuth by 60° will damp the TE_{11} and TE_{21} modes.

2.3 Slotted High-Harmonic Gyro-TWT Amplifiers

Since axis-encircling electrons are in resonance with the s^{th} -order azimuthal mode of cylindrical waveguide when $\omega = s\Omega_c + k_{\parallel}v_{\parallel}$, high-harmonic gyrotron interaction offers the important advantage of a significantly reduced magnetic field requirement. To compensate for the weaker interaction, one can introduce an azimuthally corrugated interaction structure [8-10] which ripples the rf field lines in a way to strengthen a particular harmonic field component. The magnetron-like slotted structure is shown in Fig. 9. The number of vanes, N , is chosen such that the strongest azimuthal field harmonic is equal to the desired cyclotron harmonic number s . As in the magnetron, the modes of interest are the 2π mode, where the phase in each slot is identical, and the π mode, where adjacent slots are out of phase by π . The π mode is more ideal for the harmonic gyro interaction because a high-order ($N/2$) azimuthal mode is dominant, whereas most of the energy of the 2π mode is wasted in the useless TE_{01} mode. To obtain a strong interaction, the inner vane radius a is chosen to be fairly close to the electron Larmor radius and the outer vane radius b is then chosen to obtain the correct cutoff frequency.

2.3.1 Linear Stability Theory

A low magnetic field, moderate voltage gyrotron amplifier has been designed for stable, high performance operation at 95 GHz. A slotted interaction circuit is utilized to achieve strong amplification near the third cyclotron harmonic frequency. The start-oscillation conditions were determined by analytical theory and confirmed by Dr. A.T. Lin's multi-mode Particle-in-Cell simulation code. The dominant threat to the amplifier's stability is from a third-harmonic peniotron backward-wave interaction. Because of this peniotron mode, it became necessary to redesign our initial amplifier design. A slow-timescale particle-tracing simulation code predicts the three-section, slotted third-harmonic gyro-TWT, which utilizes an 11.6 kG magnet and a 50 kV, 3 A, $v_{\perp}/v_z = 1.4$, axis-encircling electron beam with an axial velocity spread of 6%, will yield an output power of 30 kW with an efficiency of 20%, a saturated gain of 40 dB and a constant-drive bandwidth of

2%. Varian has used this design to fabricate their 95 GHz gyro-TWT amplifier. A theoretical stability analysis for this amplifier was presented in the paper, "Stability of a 95 GHz Slotted Third-Harmonic Gyro-TWT Amplifier," by C.K. Chong, D.B. McDermott, A.T. Lin, W.J. DeHope, Q.S. Wang and N.C. Luhmann, Jr., which was submitted to the *IEEE Trans. on Plasma Science's Special Issue on High Power Microwave Generation*.

If the forward-wave amplification bandwidth of a gyro-TWT is sufficiently broad to extend into the negative- k_z region, then gain exists for waves propagating counter to the electron beam, which represents internal feedback. Wave growth is no longer convective, but rather grows absolutely in time (oscillation) [11]. The onset of the absolute instability is found as the minimum beam-wave coupling value at which infinite growth rate occurs for an infinitesimally small, positive value of k_z . Figure 10 shows the threshold beam current for the absolute instability in the slotted gyro-TWT as a function of the beam's velocity ratio $v_{\perp}/v_z (\equiv \alpha)$. The amplifier is much more susceptible to the absolute instability for larger values of α .

In addition to oscillations in the operating mode due to the absolute instability, a slotted gyro-TWT can also oscillate in other modes due to backward-wave oscillations [12] at various cyclotron harmonics. If the magnetic field is adjusted so that a grazing intersection is established between the π mode and the third-harmonic cyclotron resonance line, then gyro-BWO oscillations can occur if the s^{th} cyclotron harmonic resonance line intersects with any mode with negative- k_z that contains an azimuthal harmonic number $\Gamma = s$ and if the interaction length is sufficiently long. Also, penio-BWO oscillations [13] can occur where the s^{th} -harmonic resonance line intersects with a mode that contains $\Gamma = s+1$. From the dispersion diagram in Fig. 11, the potential gyro-BWO oscillations are in the $2\pi/3$, $\pi/3$, and 2π modes at the fourth, fifth, and sixth harmonics, respectively. It is also evident in Fig. 11 that the third-harmonic resonance line intersects the $2\pi/3$ mode in the negative- k_z region close to its cutoff, which is the ideal situation for oscillation. An asynchronous third-harmonic peniotron interaction [10,13-15] can potentially grow at this intersection. Using the linear theory that was presented in Ref. 16, the start-oscillation conditions can be determined by performing a two-dimensional search in both frequency and length. The analytical theory in Ref. 16 accounts for both the gyrotron and peniotron interactions. The peniotron interaction involves a drift of the guiding centers. The values of the critical gyro-BWO and penio-BWO start-oscillation lengths for the parameters listed in Table I are shown in Fig. 12. It is evident that the penio-BWO is the strongest threat to the amplifier's stability and that the fourth-harmonic, $2\pi/3$ -mode gyro-BWO is the next strongest. The fifth-harmonic, $\pi/3$ -mode interaction is fairly weak because the intersection occurs far above the cutoff frequency. Velocity spread effects will quench this interaction further. For the design parameters listed in Table I, the critical length of the third-harmonic, $2\pi/3$ -mode penio-BWO from the linear theory is 4.5 cm.

Dr. A.T. Lin's time-dependent, multimode particle-in-cell (PIC) code [17,18], which has been used successfully to study the stability of smooth-wall gyro-TWT's [18,19], was modified for

simulating the performance of high-harmonic gyro-TWT's in slotted waveguide to verify the amplifier's stability. The code retains hundreds of longitudinal modes for each of several transverse modes, and follows the spatial and temporal evolution of the beam-wave interactions self-consistently. The behavior of the absolute instability is described in Fig. 13, where it is seen that the proposed amplifier will oscillate for an electron beam current of 3.5 A, in rough agreement with the predictions in Fig. 10. The PIC code has also been used to study the threshold conditions for the penio-BWO and gyro-BWO modes. The starting conditions for the amplifier's primary oscillation threat, the third-harmonic penio-BWO, is shown in Fig. 14. For the parameters in Table I, it is found that the penio-BWO is on the verge of oscillation for an interaction length of 4.5 cm, in good agreement with the analytical results in Fig. 12. The critical oscillation lengths for the gyro-BWO modes are longer.

The previous stability analyses have found that all possible oscillations in the slotted gyro-TWT described in Table I will be suppressed for an interaction length less than 4.5 cm. To create a safety margin, the longest interaction length for the 95 GHz amplifier circuit is chosen to be 4.0 cm. However, since a single section with this length will not yield the desired gain of greater than 30 dB, the proposed amplifier contains three interaction sections separated by attenuating severs [2,20] for rf isolation. The nonlinear self-consistent, particle-tracing simulation code [10,21] that was used to benchmark the linear theory in Fig. 15 was also used to evaluate the saturated characteristics of the proposed 95 GHz, three-section amplifier described in Table I. The predicted spatial power profile of a 93.2 GHz wave in the severed amplifier is shown in Fig. 16. The proposed 95 GHz, slotted third-harmonic gyro-TWT amplifier with an 11.6 kG magnet and a 50 kV, 3 A, $\alpha=1.4$, $\Delta v_z/v_z=6\%$, axis-encircling electron beam is predicted to generate a peak power of 30 kW with 20% efficiency, a 40 dB saturated gain and a 3 dB constant-drive bandwidth of 2.0%, as shown in Fig. 17.

2.3.2 Third-Harmonic Slotted Gyro-TWT Experiment

Our first operation of a slotted third-harmonic gyrotron traveling-wave amplifier has been reported in a paper submitted to the *IEEE Trans. of Plasma Science's Special Issue on High Power Microwave Generation* ("Slotted Third-Harmonic Gyro-TWT Amplifier Experiment," by C.K. Chong, D.B. McDermott and N.C. Luhmann, Jr.). The low magnetic field, moderate voltage gyrotron amplifier's 61 keV, 2.5 A, $v_\perp/v_z = 1.0$, axis-encircling electron beam was supplied by a gyroresonant RF accelerator [22]. The 10 GHz, 1.1 kG, single-section, slotted third-harmonic amplifier is stable and yielded 13 dB of small-signal gain with a bandwidth of 3%. The experiment was performed as a scaled test of Varian's planned 95 GHz, multi-section slotted amplifier.

In order to test the novel 95 GHz amplifier in a more moderately sized circuit, a 10 GHz device was built that was scaled in size by a factor of nine. The primary objective of the scaled

experiment was to determine whether the 95 GHz amplifier will be stable. Therefore, the slotted gyro-TWT experiment was performed with a single interaction section equal to the scaled length of the longest section of the multi-section 95 GHz device.

2.3.2.3 Small-Signal Experimental Results

The slotted third-harmonic gyro-TWT proof-of-principle experiment was performed with a single interaction section. The parameters are given in Table II. The advantage of testing an unsevered gyro-TWT amplifier is that the input signal is directly transmitted through to the output port, which allows the gain to be determined from the ratio of the output power with the electron beam to the value without it. The 1 kW input signal from the TWT amplifier was insufficient to drive the test amplifier into saturation due to the 10 dB insertion loss from the input coupler. The constant-drive bandwidth was measured by keeping the operating parameters and the RF input power fixed and varying only the input frequency. The constant-drive bandwidth of the unsaturated one-section slotted gyro-TWT amplifier is shown in Fig. 17, where the gain represents the interaction gain and not the device gain. The small-signal gain is 13 dB and the bandwidth is 3%. Figure 18 also shows the bandwidth predicted by the simulation code [21]. The amplifier was found to be stable.

2.3.2.4 Large-Signal Test Preparation

The large-signal hot-tests of the slotted third-harmonic gyro-TWT can now be performed because we have improved the efficiency of our input and output couplers. Another set of couplers was fabricated based on our HFSS [23] simulation runs of a modified design. The coupling has been increased from 10 dB to 5 dB which is sufficient for driving the interaction into saturation with our 1 kW helix TWT driver.

In addition, to improve the device's stability by using the same slicing technique that was successfully employed in our second-harmonic smooth-bore gyro-TWT, a new mode-selective interaction circuit has been fabricated for the slotted gyro-TWT. The new slotted circuit has been cut with three cuts separated in azimuth by 120° to suppress all modes except for the operating π mode. This will suppress the gyrofrequency multiplier emission and the fourth-harmonic gyro-BWO emission in the $4\pi/3$ mode, as well as the third-harmonic penio-BWO that was predicted by theory to be the dominant stability threat.

We have begun to make the initial alignment hot-tests of the slotted third-harmonic gyro-TWT amplifier upgrade.

2.4 Third-Harmonic Gyrotron Reflection Amplifier

We have utilized the basic principle that any rf oscillator can be employed as a reflection amplifier to design a lightweight 35 GHz gyrotron amplifier. A reflection amplifier is operated just under the start-oscillation condition. High efficiency is predicted for our 50 kV, third-harmonic gyrotron design. Operation at the third harmonic allows the required magnetic field for 35 GHz generation to be supplied by a 4.5 kG permanent magnet. Two gyrotrons employing sliced circuits for mode control have been evaluated with a nonlinear code and found to be capable of producing 25 kW continuously. A third-harmonic TE_{41} gyrotron utilizing a magnetron injection electron gun is predicted to yield 46% device efficiency with a single-stage depressed collector and 17% without one, while a more ideal axis-encircling electron beam from a Cusp electron gun can drive a third-harmonic TE_{31} gyrotron with a device efficiency of 23%, which can be increased to 45% through the use of a depressed collector. The theoretical principles, design and evaluation of our compact third-harmonic gyrotron was described in the paper, "35 GHz, 25 kW CW Third-Harmonic Gyrotron," by D.B. McDermott, A.J. Balkcum and N.C. Luhmann, Jr., which was submitted to the *IEEE Trans. on Plasma Science's Special Issue on High Power Microwave Generation*.

The harmonic gyrotron interaction strength increases with voltage. However, for applications where size and weight are a premium, it is desirable to minimize the operating voltage. Fortunately, the interaction is sufficiently strong at the moderately low voltage of 50 kV for $v_{\perp}/v_z = 2$.

For m^{th} -harmonic gyrotrons, the interaction is strongest for an axis-encircling electron beam and a TE_{m1} mode. The dependence of the third-harmonic coupling coefficient [24] on the guiding-center radius is shown in Fig. 19 for $m = s$ and $m = s \pm 1$. For an annular beam with finite r_c , mode numbers with $m \neq s$ may yield stronger interaction than for $m = s$.

The dispersion diagrams for the proposed $TE_{31}^{(3)}$ and $TE_{41}^{(3)}$ gyrotrons (the superscript refers to the harmonic number) are shown in Fig. 20, where it has been assumed that the cavities have been sliced to suppress modes without the desired m^{th} -order azimuthal symmetry by interrupting their azimuthal wall currents, which was successfully employed in a $TE_{41}^{(4)}$ gyrotron experiment [6] and in a recent $TE_{21}^{(2)}$ gyro-TWT experiment [25].

To evaluate and optimize the designs, a nonlinear code [26] was used that numerically integrates the equations of motion for electrons propagating through a cavity in the presence of a linearly tapered magnetic field and the electromagnetic fields of a linearly polarized TE_{mn} mode. After the conversion efficiency is found from the average energy loss of the beam, the electron beam current is given by the power balance equation. The code properly accounts for the mechanisms in a gyrotron oscillating at a single frequency, except for the higher order effect of profile modification of the mode by the electron beam.

2.4.1 $TE_{31}^{(3)}$ Gyrotron Reflection Amplifier with a Cusp Gun

A $TE_{31}^{(3)}$ gyrotron with the parameters listed in Table III(a) has been designed for a 50 kV, 2.2 A, $v_{\perp}/v_z = 2$, axis-encircling beam from a Cusp electron gun [27]. As shown in Fig. 21(a), the predicted conversion efficiency is 31%, yielding a device efficiency of 23% for an output power of 25 kW. The magnetic field has been linearly uptapered by 1.3% over the length of the cavity to enhance the efficiency. A relatively large axial velocity spread of 30% would only reduce the conversion efficiency from 31% to 30%. Since the lowest energy of the spent beam is 25 keV, a 25 kV single-stage depressed collector would increase the efficiency to 45%. CW operation can be sustained since the average ohmic cavity wall-loading is 0.29 kW/cm^2 , which is considerably less than the typical limit of 2 kW/cm^2 for high power CW gyrotrons. To transform the TE_{31} output wave into the fundamental mode, a four-period linearly polarized TE_{31}/TE_{11} mode converter [4] with an azimuthal perturbation of $m_c = 4$ has been developed [5] with a measured conversion efficiency of 98%.

2.4.2 $TE_{41}^{(3)}$ Gyrotron Reflection Amplifier with a MIG Gun

A $TE_{41}^{(3)}$ gyrotron with the parameters listed in Table III(b) has been designed for a 50 kV, 3.0 A, $v_{\perp}/v_z = 2$, annular beam from a MIG. As shown in Fig. 21(b), it is capable of generating 25 kW with a conversion efficiency of 25% and a device efficiency of 17%. A 1.3% linear magnetic uptaper has also been used. A 30% velocity spread would only reduce the conversion efficiency from 25% to 23%. The efficiency can be boosted to 46% by employing a 32 kV depressed collector. This gyrotron has an ohmic wall loading of 0.21 kW/cm^2 when operated CW. A TE_{41}/TE_{11} mode converter [5] has been tested with a conversion efficiency of 98.4%.

3. References

- [1] D.S. Furuno, D.B. McDermott, C.S. Kou, N.C. Luhmann, Jr., and P. Vitello, "Theoretical and Experimental Investigation of a High-Harmonic Gyro-Travelling Wave Tube Amplifier," *Phys. Rev. Lett.* **62**, 1314 (1989).
- [2] A.T. Lin, K.R. Chu, C.C. Lin, C.S. Kou, D.B. McDermott, and N.C. Luhmann, Jr., "Marginal Stability Design Criterion for Gyro-TWT's and Comparison of Fundamental with Second Harmonic Operation," *Int. J. Electron.*, vol. 72, pp. 873-885, 1992.
- [3] Q.S. Wang, C.S. Kou, D.B. McDermott, A.T. Lin, K.R. Chu, and N.C. Luhmann, Jr., "High-Power Harmonic Gyro-TWT's--Part II: Nonlinear Theory and Design", *IEEE Trans. on Plasma Science*, **20**, pp. 163-169, 1992.
- [4] C. Moeller, "Mode Converters Used in the Doublet III ECH Microwave System," *Int. J. Electronics*, vol. 53, no. 6, pp. 587-393, 1982.
- [5] D.B. McDermott, J. Pretterebner, C.K. Chong, C.F. Kinney, M.M. Razeghi, and D.B. McDermott, "Broadband Linearly-Polarized Beat-Wave TE_{m1}/TE_{11} Mode Converter," to be published, *IEEE Microwave Theory and Tech.*, January, 1996.
- [6] D.B. McDermott, N.C. Luhmann, Jr., D.S. Furuno, A. Kupiszewski, and H.R. Jory, "Operation of a Millimeter-Wave Harmonic Gyrotron," *Int. J. of Infrared and Millimeter Waves* **4**, 639 (1983).
- [7] Q.S. Wang, D.B. McDermott, A.T. Lin, N.C. Luhmann, Jr., and J. Pretterebner, "35 GHz High Power, Second Harmonic Gyro-TWT Amplifier," *Tech. Digest of IEEE Int. Electron Devices Meeting*, pp. 207-210, 1992.
- [8] Y.Y. Lau and L.R. Barnett, "Theory of a Low Magnetic Field Gyrotron (Gyromagnetron)," *Int. J. Infrared and Millimeter Waves*, vol. 3, no. 5, pp. 619-643, 1982.
- [9] K.R. Chu and D. Dialetis, "Kinetic Theory of Harmonic Gyrotron Oscillation with Slotted Resonant Structure," in *Infrared and Millimeter Waves*, vol. 13, New York Academic Press, 1985, pp. 45-75.
- [10] A.K. Ganguly, S. Ahn, and S.Y. Park, "Three Dimensional Theory of the Gyropeniotron Amplifier," *Int. J. Electron.*, vol. 65, no. 3, pp. 597-618, 1988.
- [11] Y.Y. Lau, K.R. Chu, L.R. Barnett, and V.L. Granatstein, "Gyrotron Travelling Wave Amplifier: I. Analysis of Oscillations," *Int. J. Infrared and Millimeter Waves*, vol. 2, pp. 373-393, 1981.
- [12] S.Y. Park, V.L. Granatstein, and R.K. Parker, "A Linear Theory and Design Study for a Gyrotron Backward Wave Oscillator," *Int. J. Electron.*, vol. 57, pp. 1109-1123, 1984.
- [13] A.T. Lin and C.C. Lin, "Peniotron Forward-Wave Self-Oscillation," *Applied Phys. Lett.*, vol. 64, pp. 1088-1090, 1994.
- [14] S. Ono, K. Tsutaki, and T. Kageynama, "Proposal of a High Efficiency Tube for High Power Millimeter or Submillimeter Wave Generation: The Gyro-Peniotron," *Int. J. Electron.*, vol. 56, pp. 507-520, 1984.
- [15] P. Vitello, "Cyclotron Maser and Peniotron-Like Interactions in a Whispering Gallery Mode Gyrotron," *IEEE Trans. on Microwave Theory. and Tech.*, vol. MTT-32, pp. 917-921, 1984.
- [16] C.K. Chong, D.B. McDermott, A.T. Lin, W.J. DeHope, Q.S. Wang and N.C. Luhmann, Jr., "Stability of a 95 GHz Slotted Third-Harmonic Gyro-TWT Amplifier," submitted to *IEEE Trans. on Plasma Science*.
- [17] J.M. Dawson and A.T. Lin, *Basic Plasma Physics*, vol. II, M.N. Rosenbluth and R.Z. Sagdeev, Eds., North Holland, Amsterdam, The Netherlands, 1984, ch. 7.
- [18] A.T. Lin, M. Caplan, and K.R. Chu, "A Study of Saturated Output of a TE_{01} Gyrotron Using an Electromagnetic Finite Size Particle Code," *Int. J. Electron.*, vol. 53, p. 659, 1982.

- [19] A.T. Lin and P.K. Kaw, "Absolute Instability in Finite Length Cyclotron Maser Systems," *Int. J. Electron.*, vol. 72, p. 887, 1992.
- [20] A.K. Ganguly and S. Ahn, "Self-Consistent Large Signal Theory of a Gyrotron Traveling Wave Amplifier," *Int. J. Electron.*, vol. 53, p. 505, 1982.
- [21] C.K. Chong, D.B. McDermott, A.T. Balkcum, N.C. Luhmann, Jr., "Nonlinear Analysis of High-Harmonic Slotted Gyro-TWT Amplifier," *IEEE Trans. on Plasma Science*, vol. 20, no. 3, pp. 176-87, 1992.
- [22] D.B. McDermott, D.S. Furuno, and N.C. Luhmann, Jr., "Production of Relativistic, Rotating Electron Beams by Gyroresonant RF Acceleration in a TE₁₁₁ Cavity," *J. Appl. Physics*, vol. 58, no. 12, pp. 4501-4508, 1985.
- [23] "HP High-Frequency Structure Simulator," HP Part No. 85180-90037, Hewlett-Packard Co. and Ansoft Co., May 1992.
- [24] K.R. Chu and A.T. Lin, "Gain and Bandwidth of the Gyro-TWT and CARM Amplifiers," *IEEE Trans. Plasma Sci.* 16, 90 (1988).
- [25] Q.S. Wang, K.C. Leou, C.K. Chong, A.J. Balkcum, D.B. McDermott, and N.C. Luhmann, Jr., "Gyro-TWT Amplifier Development at UCD," *Digest of 19th Int. Conf. on Infrared and Millimeter Waves*, Sendai, Japan, 1994.
- [26] K.R. Chu, M.E. Read, and A.K. Ganguly, "Methods of Efficiency Enhancement and Scaling for the Gyrotron Oscillator," *IEEE Trans. on MTT*, 28, 318 (1980).
- [27] N.R. Vanderplaats, H.E. Brown, and S. Ahn, "Magnetically Shielded Electron Guns with a Center Magnetic Post," *Tech. Dig. IEDM*, 336 (1981).

4. Figures and Tables

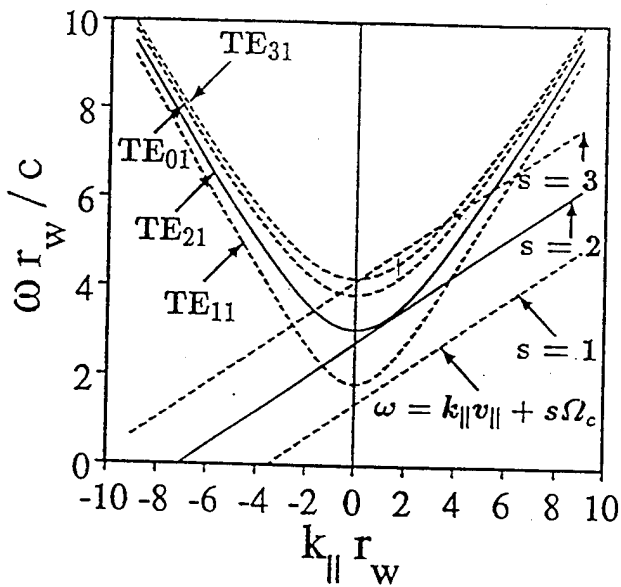


Fig. 1. Uncoupled dispersion relation of the operating mode (intersection of unbroken curves) and possible oscillating modes (intersections of broken curves with negative k_{\parallel}) for the $TE_{21}^{(2)}$ gyro-TWT amplifier.

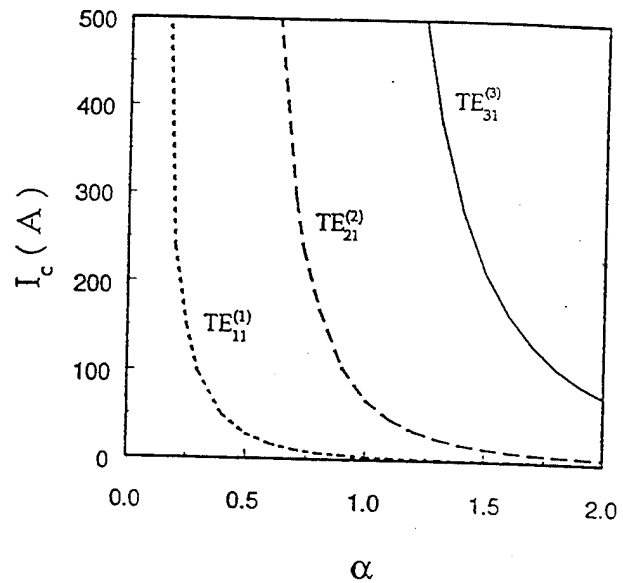


Fig. 2. Dependence of the critical current for absolute instability on the velocity ratio $\alpha = v_{\perp} / v_{\parallel}$ in fundamental, second and third harmonic $TE_{n1}^{(n)}$ gyro-TWT amplifiers (80 kV, $B/B_g = 0.97$, and $r_c/r_w = 0.4$).

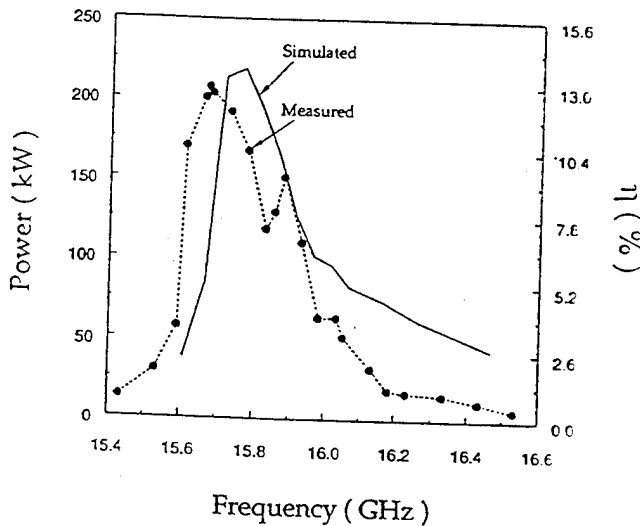


Fig. 3. Saturated bandwidth of the $TE_{21}^{(2)}$ gyro-TWT amplifier (80 kV, 20 A, $B/B_g = 0.97$) from measurement (solid points and broken line) and simulation (solid curve).

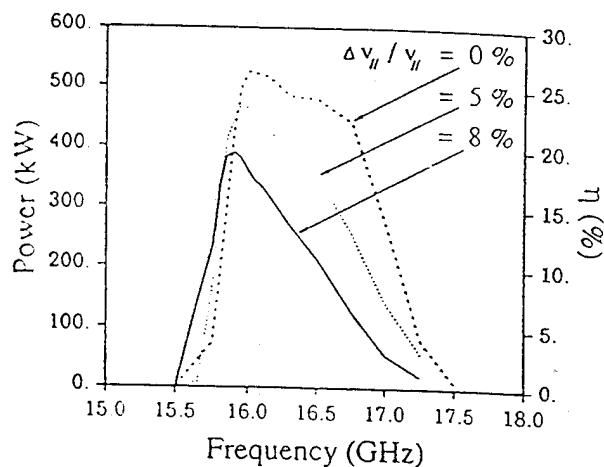


Fig. 4. Constant-drive bandwidth of the $TE_{21}^{(2)}$ gyro-TWT amplifier (100 kV, 20 A, $B/B_g = 0.98$) from simulation for several values of axial velocity spread.

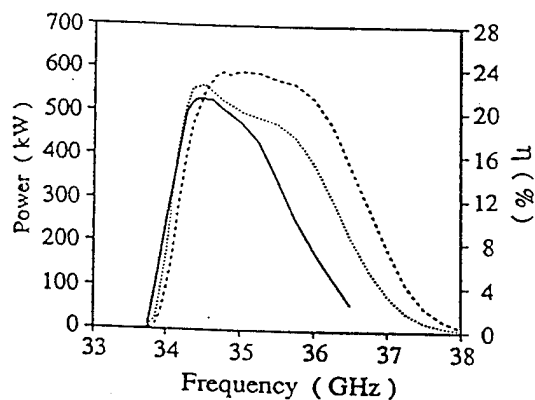


Fig. 5. Constant-drive bandwidth of the $TE_{21}^{(2)}$ gyro-TWT amplifier (100 kV, 25 A, $B/B_g=0.98$) from simulation for an axial velocity spread of 0% (dashed curve), 3% (dotted curve), and 5% (solid curve).

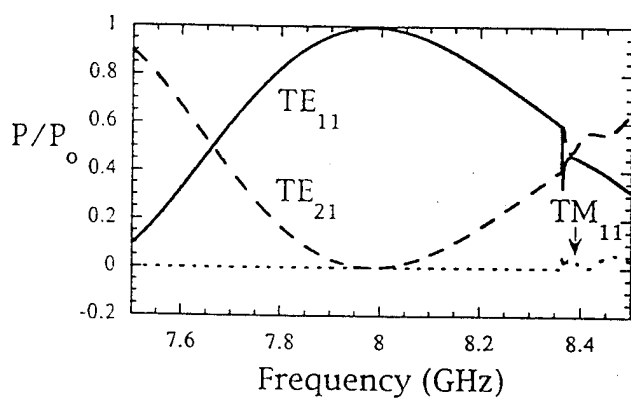


Fig. 7. Dependence on frequency of power distribution in the TE_{21} (dashed line), TE_{11} (solid line), and TM_{11} (dotted line) modes from simulation for wave emanating from the four-period $m_c=3$ converter and normalized to power of TE_{21} input wave.

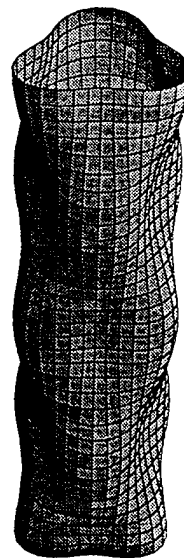


Fig. 6. Schematic of a two-period $m_c = 3$ TE_{21}/TE_{11} beat-wave mode converter.

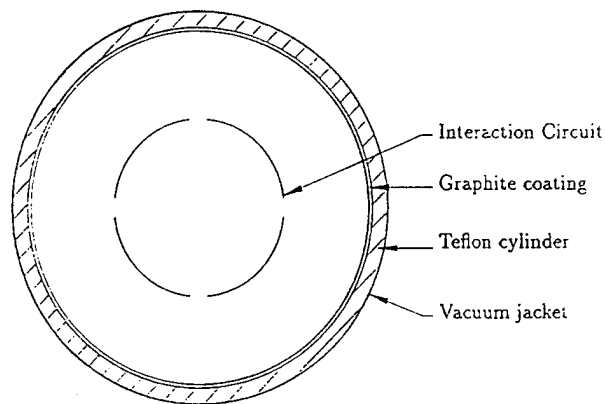


Fig. 8. Cross section of the sliced interaction circuit surrounded by a lossy dielectric tube.

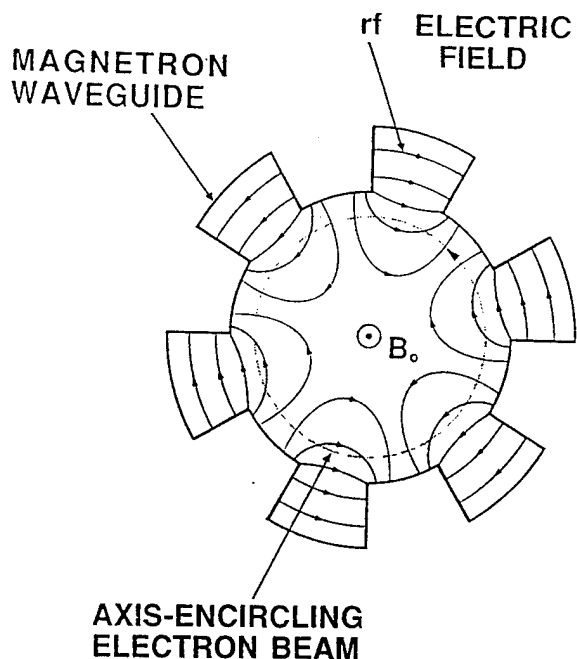


Fig. 9. Cross-sectional view of the slotted gyro-TWT with six vanes and showing the rf electric field pattern of the π mode.

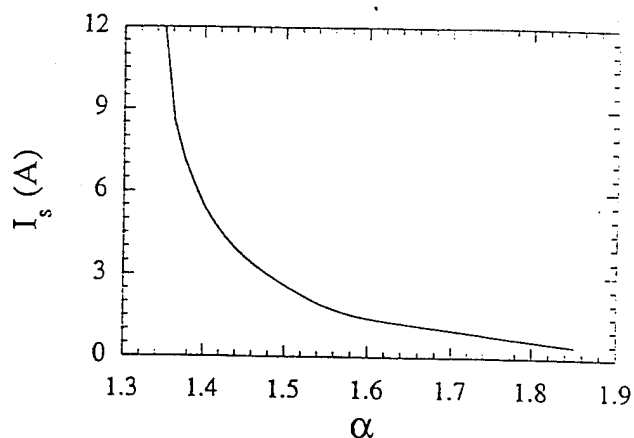


Fig. 10. Dependence of the threshold-oscillation current on velocity ratio $\alpha = v_{\perp}/v_z$ for absolute instability [Table I, $B/B_g = 0.995$].

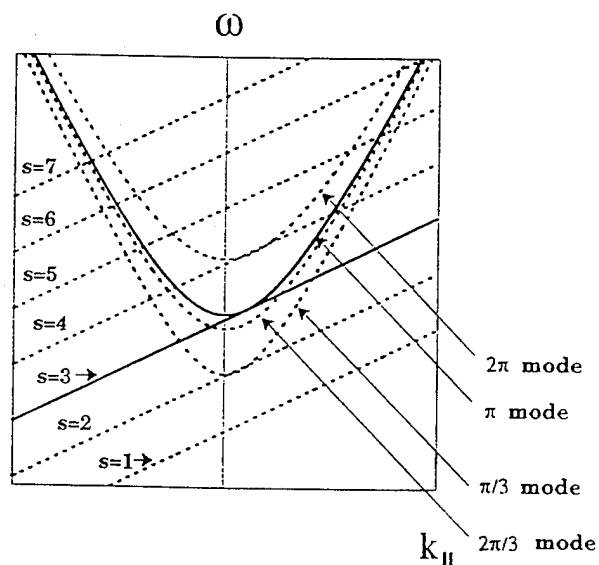


Fig. 11. Uncoupled dispersion relation of the operating mode (intersection of unbroken curves) and potential oscillating modes (intersections of broken curves with negative k_z) for the slotted third-harmonic gyro-TWT amplifier [Table I].

Table I. Design parameters for the three-section 95 GHz, slotted third-harmonic gyro-TWT amplifier.

| | |
|---------------------------|------------------------|
| Beam Voltage | 50 kV |
| Beam Current | 3 A |
| v_{\perp}/v_z | 1.4 |
| $\Delta v_z/v_z$ | 6% |
| Magnetic Field | 11.58 kG |
| B/B_g | 0.99 |
| Cyclotron Harmonic | 3 |
| Mode | π mode |
| Number of Vanes | 6 |
| $\omega_c/2\pi$ | 92.23 GHz |
| r_{\perp}/a | 0.52 |
| r_{\parallel}/a | 0.0 |
| $\Delta r_{\parallel}/a$ | 10% |
| Inner Circuit Radius, a | 1.037 mm |
| Outer Circuit Radius, b | 1.474 mm |
| Interaction Lengths | 3.0 cm, 3.0 cm, 4.0 cm |
| Sever Lengths | 0.6 cm, 1.0 cm |
| Circuit Length | 11.6 cm |

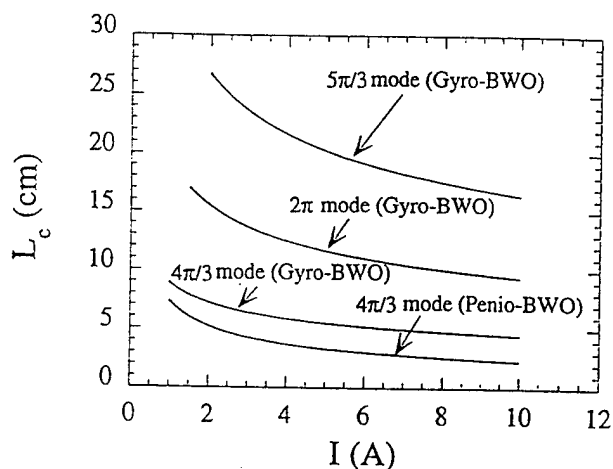


Fig. 12. Dependence of the critical-oscillation length on beam current for gyro-BWO at the fourth, fifth and sixth harmonics in the $2\pi/3$, $\pi/3$ and 2π modes, respectively, and third-harmonic penio-BWO in the $2\pi/3$ mode [Table I].

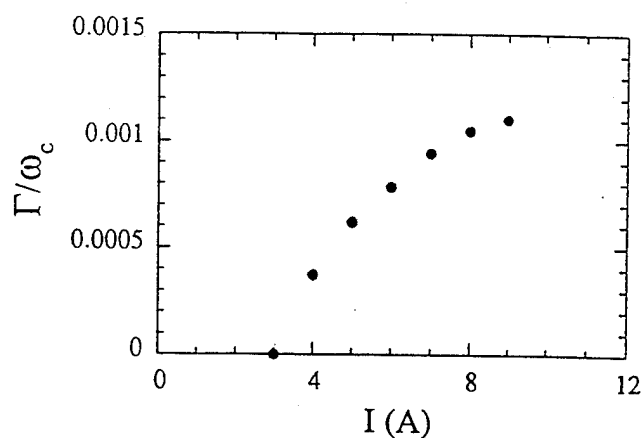


Fig. 13. Predicted PIC code dependence on the electron beam current of the absolute instability's growth rate normalized to the cutoff frequency [Table I with $L = 10$ cm].

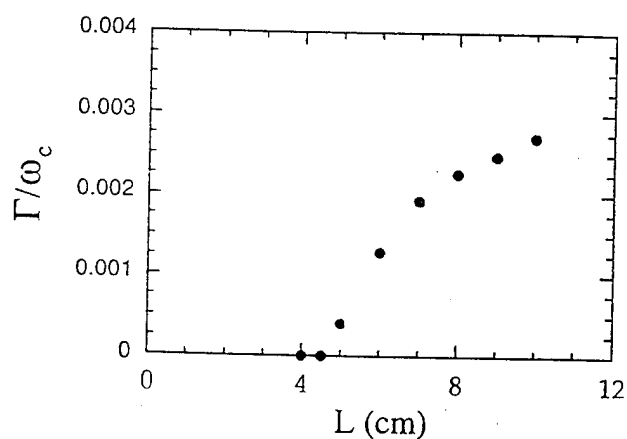


Fig. 14. Predicted PIC code dependence on the interaction length of the third-harmonic penio-BWO's growth rate normalized to the cutoff frequency [Table I].

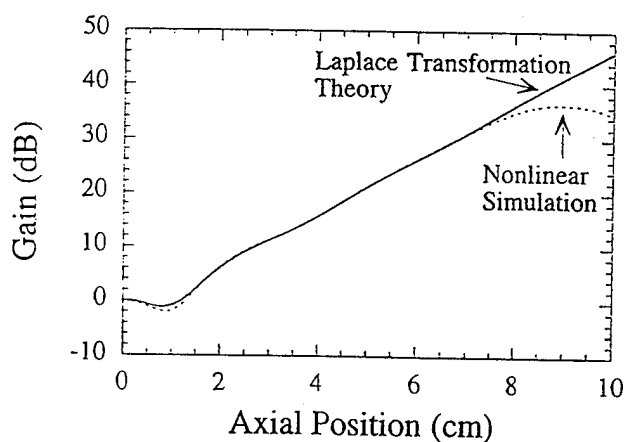


Fig. 15. Predicted spatial power profile of a 95 GHz wave in the unsevered slotted third-harmonic gyro-TWT [Table I] from linear theory (broken curve) and nonlinear simulation (solid curve).

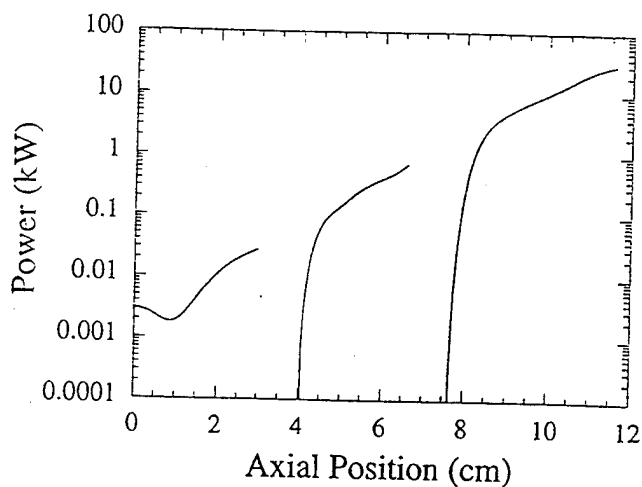


Fig. 16. Predicted spatial power profile of a 93.2 GHz wave in the three-section, slotted third-harmonic gyro-TWT amplifier [Table I, $P_{in} = 2$ W].

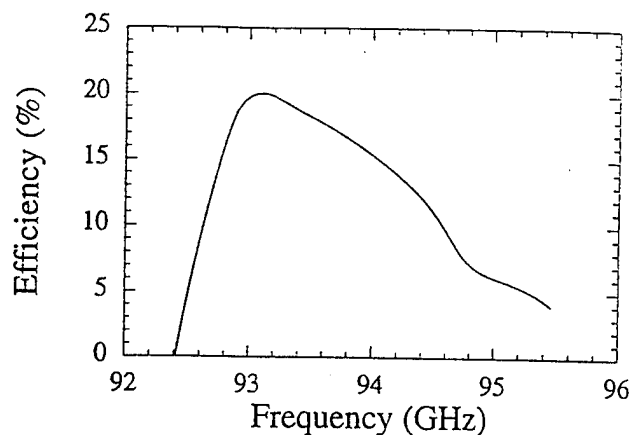


Fig. 17. Predicted constant-drive bandwidth of the three-section, slotted third-harmonic gyro-TWT amplifier [Table I, $P_{in} = 2$ W].

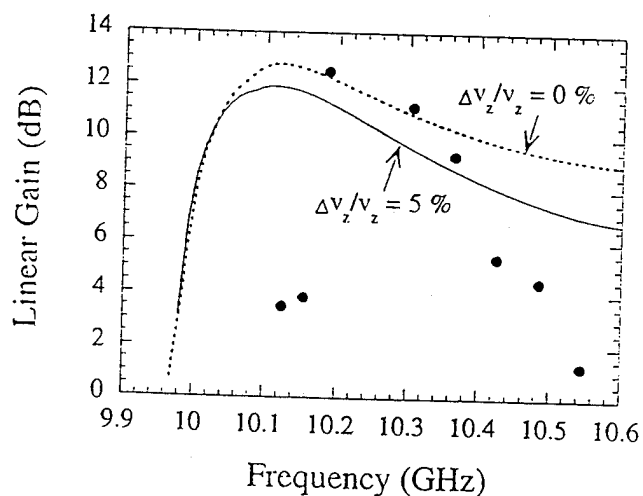


Fig. 18. Bandwidth of the small-signal interaction gain in the one-section, slotted third-harmonic gyro-TWT amplifier from measurement (filled circles) and the simulation code with velocity spreads of $\Delta v_z/v_z = 0$ and 5% (Table II).

Table II. Experimental parameters for the 10.2 GHz, single section, slotted third-harmonic gyro-TWT amplifier.

| | |
|---------------------------|------------|
| Beam Voltage | 61 kV |
| Beam Current | 2.5 A |
| v_{\perp}/v_z | 1.0 |
| Magnetic Field | 1.14 kG |
| Cyclotron Harmonic | 3 |
| Mode | π mode |
| Number of Vanes | 6 |
| $\omega_c/2\pi$ | 10.04 GHz |
| r_{\perp}/a | 0.47 |
| r_{\parallel}/a | 0.0 |
| $\Delta r_{\parallel}/a$ | 29% |
| Inner Circuit Radius, a | 0.96 cm |
| Outer Circuit Radius, b | 1.37 cm |
| Circuit Length | 37.3 cm |

Table III. Parameters for the 25 kW CW, 35 GHz third-harmonic gyrotrons using (a) a Cusp electron gun and (b) a MIG.

| | (a) | (b) |
|-----------------------------------|------------------|------------------|
| Voltage | 50 kV | 50 kV |
| Current | 2.2 A | 3.0 A |
| Velocity Ratio, v_1/v_z | 2.0 | 2.0 |
| Magnetic Field | 4.48 kG | 4.52 kG |
| Magnetic Taper | +1.3% | +1.3% |
| Cyclotron Harmonic | 3 | 3 |
| Mode | TE ₃₁ | TE ₄₁ |
| Guiding Center Radius, r_c/r_w | 0.0 | 0.35 |
| Cavity Radius, r_w | 0.574 cm | 0.725 cm |
| Cavity Length | 8.03 cm | 13.06 cm |
| Unloaded Quality Factor, Q_0 | 6000 | 6000 |
| Diffraction Quality Factor, Q_D | 2000 | 3000 |

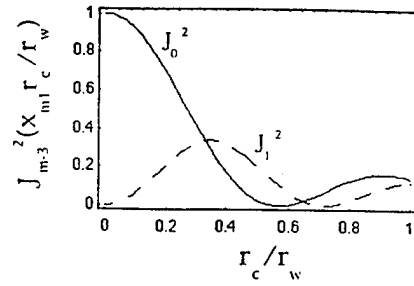


Fig. 19. Dependence of $J_{m-3}^2(x_{m1}r_c/r_w)$ on the normalized guiding-center radius of the electron beam for $m = 3$ (solid line) and $m = 4$ (dashed line).

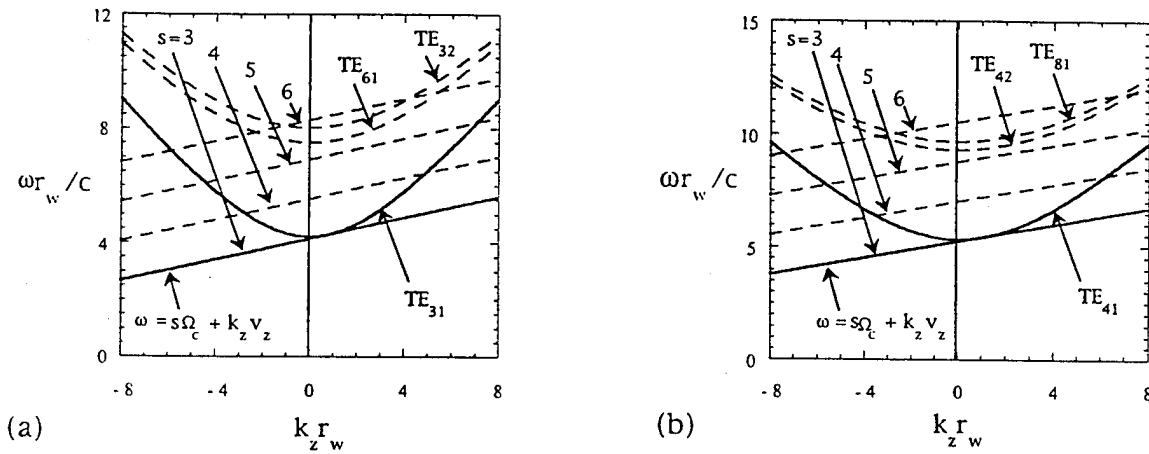


Fig. 20. Uncoupled dispersion relation of the operating mode (intersection of unbroken curves) and possible oscillating modes (intersections of broken curves) for a) $TE_{31}^{(3)}$ [Table III(a)] and b) $TE_{41}^{(3)}$ [Table III(b)] sliced gyrotrons.

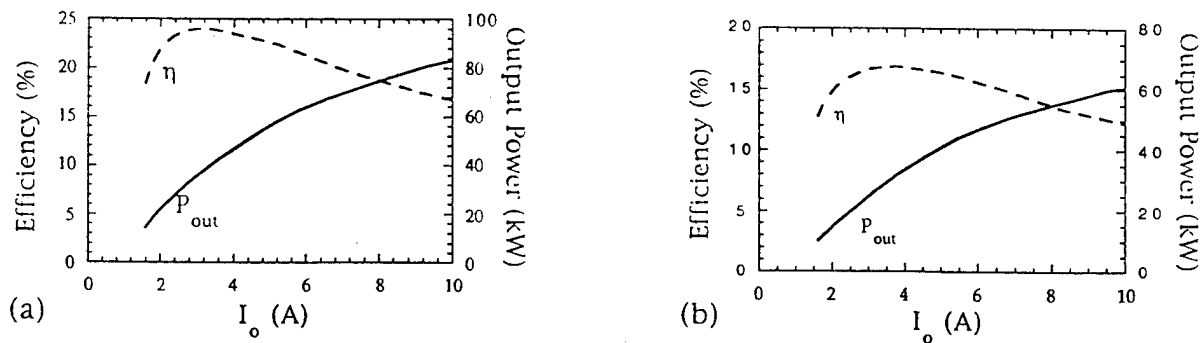


Fig. 21. Predicted dependence of output power (solid line) and device efficiency (dashed line) on the electron beam current for the third-harmonic (a) TE_{31} gyrotron [Table III(a)] and (b) TE_{41} gyrotron [Table III(b)].

5. Publications and Conference Presentations during 9/1/94 -- 8/31/95

Q.S. Wang, D.B. McDermott, C.K. Chong, C.S. Kou, K.R. Chu, and N.C. Luhmann, Jr., "Design of 1 MW, 140 GHz Third-Harmonic TE₃₁ Gyro-TWT Amplifier," *IEEE Trans. on Plasma Science*, 22, 608 (1994).

D.B. McDermott, C.K. Chong, N.C. Luhmann, Jr., K.R. Chu, and D. Dialetis, "High Harmonic Slotted Gyroklystron Amplifier: Linear Theory and Nonlinear Simulation," *IEEE Trans. on Plasma Science*, 22, 920 (1994).

Q. S. Wang, D. B. McDermott and N. C. Luhmann, Jr., "Characteristics of a Stable 200 kW Second-Harmonic Gyro-TWT Amplifier," to be published, Tech. Dig. of IEEE Int. Electron Devices Meeting, 1995.

D.B. McDermott, J. Pretterebner, C.K. Chong, C.F. Kinney, M.M. Razeghi, and D.B. McDermott, "Broadband Linearly-Polarized Beat-Wave TE_{m1}/TE₁₁ Mode Converter," to be published, IEEE Microwave Theory and Tech., January, 1996.

Q.S. Wang, D.B. McDermott and N.C. Luhmann, Jr., "Demonstration of Marginal Stability Theory by a 200 kW Second-Harmonic Gyro-TWT Amplifier," accepted for publication, Phys. Rev. Lett., October, 1995.

C.K. Chong, D.B. McDermott and N.C. Luhmann, Jr., "Slotted Third-Harmonic Gyro-TWT Amplifier Experiment," submitted to IEEE Trans. on Plasma Science, September, 1995.

C.K. Chong, D.B. McDermott, A.T. Lin, W.J. DeHope, Q.S. Wang and N.C. Luhmann, Jr., "Stability of a 95 GHz Slotted Third-Harmonic Gyro-TWT Amplifier," submitted to IEEE Trans. on Plasma Science, September, 1995.

Q. S. Wang, D. B. McDermott and N. C. Luhmann, Jr., "Operation of a Stable 200 kW Second-Harmonic Gyro-TWT Amplifier," submitted to IEEE Trans. on Plasma Science, September, 1995.

D.B. McDermott, A.J. Balkcum and N.C. Luhmann, Jr., "35 GHz, 25 kW CW Third-Harmonic Gyrotron," submitted to IEEE Trans. on Plasma Science, August, 1995.

C.K. Chong, D.B. McDermott, A.J. Balkcum, N.C. Luhmann, Jr., A.T. Lin, and W.J. DeHope, "Slotted Third-Harmonic Gyro-TWT Results," *Bull. Am. Phys. Soc.* 39, 1742 (1994).

Q.S. Wang, D.B. McDermott, A.J. Balkcum and N.C. Luhmann, Jr., "High Power, n^{th} -Harmonic TE_{n1} Gyro-TWT's: 200 kW Second-Harmonic Results and 1 MW Third-Harmonic Design," *Bull. Am. Phys. Soc.* 39, 1742 (1994).

Q.S. Wang, K.C. Leou, C.K. Chong, A.J. Balkcum, D.B. McDermott, and N.C. Luhmann, Jr., "Gyro-TWT Amplifier Development at UCD," *Digest of 19th Int. Conf. on Infrared and Millimeter Waves*, Sendai, Japan, 1994.

A.T. Lin, C.K. Chong, D.B. McDermott, A.J. Balkcum, F.V. Hartemann, and N.C. Luhmann, Jr., "Third-Harmonic Slotted Forward-Wave Peniotron," *Digest of 19th Int. Conf. on Infrared and Millimeter Waves*, Sendai, Japan, 1994.

Q.S. Wang, K.C. Leou, C.K. Chong, D.B. McDermott and D.B. McDermott, "Gyro-TWT Amplifier Development at UCD: (1) 200 kW Second-Harmonic, (2) Wideband and (3) Slotted Third-Harmonic Gyro-TWT's," submitted to 1995 Joint Conf. of IEEE Plasma Science and Fifth Beam Conference, Wisconsin, 1995.

D.B. McDermott and N.C. Luhmann, Jr., "25 kW CW Harmonic Gyrotrons for 35 and 94 GHz," submitted to APS Annual Conf. of Div. of Plasma Physics, 1995.

C.K. Chong, D.B. McDermott and N.C. Luhmann, Jr., "Third-Harmonic Slotted Gyro-TWT Operation," submitted to APS Annual Conf. of Div. of Plasma Physics, 1995.

Q.S. Wang, D.B. McDermott and N.C. Luhmann, Jr., "Operation of a 200 kW Second-Harmonic Gyro-TWT Amplifier," submitted to APS Annual Conf. of Div. of Plasma Physics, 1995.

D.B. McDermott, A.J. Balkcum and N.C. Luhmann, Jr., "35 GHz, 25 kW CW Third-Harmonic Gyrotron," submitted to Dig. of 20th Int. Conf. on Infrared and Millimeter Waves, 1995.

C.K. Chong, D.B. McDermott and N.C. Luhmann, Jr., "Operation of a Slotted Third-Harmonic Gyro-TWT Amplifier," submitted to Dig. of 20th Int. Conf. on Infrared and Millimeter Waves, 1995.

Q.S. Wang, D.B. McDermott and N.C. Luhmann, Jr., "Stable Operation of a 200 kW Second-Harmonic TE_{21} Gyro-TWT Amplifier," submitted to Dig. of 20th Int. Conf. on Infrared and Millimeter Waves, 1995.

Stable High Power Harmonic Gyrotron Amplifiers

F49620-94-1-0426

TECHNICAL PROGRESS REPORT

TO

AIR FORCE OFFICE OF SCIENTIFIC RESEARCH

Dr. Anthony T. Lin

Department of Physics
University of California, Los Angeles
Los Angeles, CA 90024-1547

September 1, 1995, to August 31, 1995

Under the support of the Tri-Services program, (Stable High Power Harmonic Gyrotron Amplifiers,) we have carried out computer simulations using particle-in-cells codes developed at UCLA to address various issues concerned with high power harmonic gyrotron amplifiers. During the period between September 1, 1995, to August 31, 1995, we had evaluated the performance of helical peniotron amplifiers in which the electron gyration is induced by a wiggler magnetic field. The potential advantages of this configuration are that it converts both beam longitudinal and transverse energy into coherent radiation, its bandwidth is rather wide, and its helical beam structure reduces the severity of mode competition. More detailed informations are contained in the appended report.

Appendix

Helical Peniotron Amplifiers

A.T. Lin and Chih-Chien Lin

Department of Physics

University of California at Los Angeles

Los Angeles, CA 90024-1547

The performance of peniotron amplifiers which use the axis-encircling beam produced by a combined solenoidal and wiggler magnetic field was investigated through computer simulations. The potential advantages of this new configuration are that it is capable of utilizing both beam longitudinal and transverse energy to amplify injected wave and reducing the severity of mode competition.

PACS number: 52.60.+h and 52.65.+z

I. Introduction

The recent advance in the technology of generating an axis-encircling beam based on rf acceleration¹ as well as a cusp magnetic field² has attracted a renewed interest in investigating the feasibility of building peniotron devices³⁻⁵. The basic gain mechanism⁶ in the conventional peniotron interaction is driven by the electron guiding center drift caused by the positive radial gradient of the electromagnetic wave field supported by a vaned waveguide immersed in a solenoidal magnetic field. If, the azimuthal mode number (n) of the wave, relates to the electron cyclotron harmonic number s by the relation $n=s+1$, then during each complete cyclotron orbit the electrons experience one complete rf field cycle and the rotating electric field slips behind the gyrating electrons by a phase shift of 2π . In doing so, all electrons regardless of their initial phases are able to move in different directions to find their own favorable phases relative to the electromagnetic wave and they also lose energy to the wave. This unique property makes the peniotron interaction inherently a high efficiency process if $\alpha=v_{\perp}/v_z$ (v is the electron velocity) is greater than 1.

The competition between the desired peniotron mode and the self-oscillating gyrotron mode in the same supporting electromagnetic structure is an important issue to be addressed. In a backward wave oscillator configuration, we have demonstrated⁷ that the peniotron interaction is capable of suppressing the gyrotron interaction independent of their respective linear electron-wave coupling strength. This occurs because the gyrotron interaction, due to its resonant nature, induces electron guiding center spread but no guiding center drift. As a result, even a saturated gyrotron mode would only reduce the growth rate of the peniotron interaction but not prevent it from being excited. In an amplifier configuration, a rising-sun structure to alleviate the mode competition problem has been proposed⁵.

In a conventional peniotron in which the electron gyrating motion is induced by

a solenoidal magnetic field, the beam-wave interaction converts only the transverse component of beam energy into coherent radiation. At the same time, part of the beam transverse energy is used in increasing the beam longitudinal energy. In the regime of $\alpha > 1$, the problem of increasing beam longitudinal energy is not very pronounced but becomes very severe as α approaches 0.5⁸. This obstacle can be overcome⁸ by using a helical beam produced by a combined solenoidal (B_0) and wiggler (B_w) magnetic field. As it is turned out, the proposed configuration also reduces the severity of mode competition.

II. Electron Equilibrium Orbit in A Combined Solenoidal And Wiggler Magnetic Field

In an earlier investigation⁹, the growth rate of peniotron interaction in an unrealizable magnetic configuration (one spatial dimension) was evaluated. Here, we make use of the following realizable static magnetic field (three spatial dimensions) to generate the axis-encircling beam.

The realizable static magnetic field can be expressed in the cylindrical coordinates (r, θ, z) by

$$\begin{aligned} \vec{B} = & B_0 \hat{e}_z + 2B_w [I_1'(k_w r) \cos(\theta - k_w z) \hat{e}_r \\ & - \frac{I_1(k_w r)}{k_w r} \sin(\theta - k_w z) \hat{e}_\theta + I_1(k_w r) \sin(\theta - k_w z) \hat{e}_z], \end{aligned} \quad (1)$$

where $k_w = 2\pi / \lambda_w$, λ_w is the wiggler period, I_n is the modified Bessel function of the first kind, and I_n' is its derivative.

The equilibrium orbit of an electron in a combined solenoidal and wiggler field has been extensively studied in microwave free electron lasers¹⁰. As was shown in

Ref. [10], the equation of motion for the transverse electron velocity can be casted in the form of a driven oscillator and its solution is

$$\begin{aligned} \vec{v}_{\perp} = & v_{\perp 0} [\cos(\bar{\Omega}_{||}t + \varphi_0) \hat{e}_x + \sin(\bar{\Omega}_{||}t + \varphi_0) \hat{e}_y] \\ & - \sum_{n=-\infty}^{\infty} v_{\perp n} \hat{e}_z \times [\sin(nk_w \bar{v}_{||}t) \hat{e}_x - \cos(nk_w \bar{v}_{||}t) \hat{e}_y], \end{aligned} \quad (2)$$

where

$$v_{\perp n} = \frac{2n\Omega_w \bar{v}_{||}}{k_w r_b (nk_w \bar{v}_{||} - \bar{\Omega}_{||})} I_n(k_w r_b) I_{n-1}(k_w r_g).$$

The first term on the right-hand side of Eq.(2) is a general solution representing the conventional cyclotron oscillation. The amplitude $v_{\perp 0}$ and phase φ_0 depend on the entrance conditions of the electron. They become negligible under adiabatic entrance conditions which implies that its competition against the self-oscillating gyrotron mode can be avoided. Ω_w and $\bar{\Omega}_{||}$ are the relativistic electron cyclotron frequency for wiggler and longitudinal fields respectively. $\bar{B}_{||} = B_0 + 2B_w I_1(k_w r_b) I_0(k_w r_g)$. $\bar{v}_{||}$ is the electron longitudinal velocity (v_z) averaged over one wiggler period, r_b and r_g are respectively the electron Larmor radius and guiding center location respectively. The second term contains oscillations at the harmonics of $k_w \bar{v}_{||}$ driven by the wiggler field. They becomes significant only for the off-axis electrons ($r_g > 0$).

In the case of electrons with axis-encircling motion ($r_g = 0$), all but the $n=1$ term vanish so

$$v_{\perp 1} \equiv \frac{2\Omega_w \bar{v}_{||}}{k_w r_b (k_w \bar{v}_{||} - \bar{\Omega}_{||})} I_1(k_w r_b) I_0(k_w r_g). \quad (3)$$

Equation (3) reveals that the electron orbit can be controlled by adjusting B_0 and B_w . The solenoidal field B_0 is not essential for generating the helical beam but it provides confinement of the beam transport and furnishes another knob to control v_{\perp} . The presence of the helical wiggler field in the interaction region tends to improve the confinement of the electron helical motion and prevents it from quickly becoming randomized. The rapid randomization of the coherent electron helical motion was observed after the wiggler field (which imparts the transverse motion to electrons) is terminated. Using the magnetic field parameters and beam voltage listed in table I, the wiggler was turned on adiabatically over six wiggler periods. The resulting electron helical spatial distribution in the interaction region is displayed in Fig. 1a. Its corresponding α is about 0.45 (Fig. 1b). The performance of signal amplification arising from the interaction of the helical beam and a vane waveguide will be described in the following section.

III. Simulation Results

The characteristic of a six vane slotted waveguide with its cross-sectional view and an axis-encircling beam shown in Fig. 2a was described in Ref. [7]. Here, we only retain the results which are relevant to our amplifier simulation. In the interaction region, the electric and magnetic fields of a transverse electric field mode^{11,12} may be written as

$$E_n = E_{Tn}(z,t) (\hat{z} \times \nabla_{\perp} C_n) \quad (4)$$

$$B_n = B_{Tn}(z,t) \nabla_{\perp} C_n + \hat{z} B_{Ln} k_{\perp} C_n, \quad (5)$$

where C_n is the local wave function

$$C_n = - \sum_{m=-\infty}^{\infty} \frac{A_{\Gamma}}{k_{\perp}} J_{\Gamma}(k_{\perp}r) e^{j\Gamma\theta} \quad (6)$$

Here $\Gamma = n + mN$, $n = 0, 1, \dots, N/2$, m is any integer, N is the number of vanes, and $A_{\Gamma} = \frac{N\theta_0}{\pi} \cdot \frac{\sin\Gamma\theta_0}{\Gamma\theta_0}$ is the enhancement factor of the slotted structure. k_{\perp} is the cutoff wavenumber which can be determined from the circuit dispersion relation

$$\sum_{\Gamma} \frac{J_{\Gamma}(k_{\perp}a)}{J'_{\Gamma}(k_{\perp}a)} \left(\frac{\sin\Gamma\theta_0}{\Gamma\theta_0} \right)^2 = - \frac{\pi}{N\theta_0} \frac{Z_0(k_{\perp}a)}{Z_1(k_{\perp}a)}, \quad (7)$$

where Z_{Γ} is a combination of Bessel function (J_{Γ}) and Neumann function (N_{Γ}) of order Γ

$$Z_{\Gamma}(x) = J_{\Gamma}(x) - \frac{J_1(k_{\perp}b)}{N_1(k_{\perp}b)} N_{\Gamma}(x), \quad (8)$$

and $\theta_0 = 2\pi / 4N$. Here a and b denote respectively the inner and outer circuit radius. For each value of n , there are an infinite number of solutions from Eq.(7). The first root is the most important one and the associated mode is usually designated by TE_{n1} . The mode number n is also the number of times the RF field pattern repeats in one rotation around the waveguide axis. There are many possible modes but the two most interesting cases are the π mode, where adjacent slots are out of phase by π , and the 2π mode, where the phase in each slot is identical. Only the π mode is retained in our amplifier simulations. Using the parameters of Table I, the dispersion curves of the relevant waveguide modes are shown in Fig. 2b. Here, the cutoff frequency of each

mode was determined from Eq.(7) and $\omega_c = k_{\perp} c/a$. (k_{\perp} is the cutoff wavenumber for the TE₃₁ mode.)

The modes supported by the slotted structure can interact with an axis-encircling electron beam through the relativistic gyrotron, free electron laser, and non-relativistic peniotron mechanisms. The gyrotron interaction can be avoided by adiabatically turning on the wiggler field. The resonant condition between electrons propagating in a wiggler field and an electromagnetic wave can be expressed as

$$\omega = (k_z + mk_w)v_z, \quad (9)$$

where m is the wiggler harmonic number. The first three wiggler harmonic ($m=1,2,3$) lines are also plotted in Fig. 2b. For free electron laser interactions m must equals to n . As was illustrated in Eq. (2), only the $v_{\perp 1}$ component is not zero for an axis-encircling beam. By properly choosing the parameters, the $m=1$ line can be placed well below the dispersion curve of the TE₁₁ mode. By doing so, the free electron laser interaction can also be totally eliminated. In the peniotron interaction, the rotation speed of the wave must be slower than the electron gyrating speed such that $n=m+1$. The equivalent gyration period of the electron helical motion induced by a wiggler magnetic field is given by $T=2\pi/k_w v_z$. In order to optimize the gain and bandwidth of the peniotron amplification process, the parameters are chosen to render the second harmonic wiggler beam line to become tangent to the TE₃₁ dispersion curve. All three transverse modes were included in simulations to make sure the system is stable against all the potential self-oscillating modes. No absolute unstable modes were observed. In carrying out the simulation, the outgoing wave boundary condition were imposed.

The axial spatial distribution of an signal ($P_{in}=15kW, f_0=30GHz$) injected at $z=0$ is

shown in Fig. 3a. The entire interaction region, displays first a region affected by the launching loss, followed by a linear growth region, and finally a nonlinear saturation region. The linear gain and nonlinear efficiency determined from Fig. 3a are respectively 1.6dB per cm. and 25%. Both are better than the gain and efficiency from the conventional harmonic free electron laser interaction. In order to confirm that the observed amplification process is derived from the helical peniotron interaction, the electron kinetic energy versus the axial distance at $\omega_c t = 400$ is shown in Fig. 3b. The result illustrates that all electrons collected at $z=L$ lose energy to the wave. This is the signature of the peniotron interaction which is in contrast to the gyrotron and free electron laser interactions. The laser and gyrotron interactions result in that only part of the electrons are in the right phase to convert their energy to the wave.

By injecting a test electron at $z=0$ ($\omega_c t = 400$) with the same velocity as the beam electron and following its behavior as it travels through the interaction region, more information concerning the electron-wave interaction can be obtained. Figure 4a shows the scalar product of the electron velocity and the wave electric field ($\vec{v} \cdot \vec{E}$) versus the axial distance. Positive ($\vec{v} \cdot \vec{E}$) indicates that the electron absorbs energy from the wave whereas negative ($\vec{v} \cdot \vec{E}$) shows that the electron gives up its energy to the wave. The simulation result illustrates that on the average the electron converts its kinetic energy to the wave in each helical period. The wiggle behavior of Fig. 4a is caused by the electron never remaining at a constant phase with respect to the spatially varying wave. The electron transverse spatial trajectory plot (Fig. 4b), (points represented by triangle and circle are respectively the electron entrance and exit radial positions respectively.) illustrates that in the high field region, the peniotron interaction tends to drift the center as well as diminish the radius of the electron helical motion.

Since a conventional peniotron interaction uses part of the beam transverse

energy to increase its longitudinal energy, the output efficiency becomes rather poor when α approaches 0.5⁸. To remedy this difficulty, a helical beam can be employed. This is due to the fact that in the proposed configuration, the phase velocity of the longitudinal ponderomotive force ($\vec{v}_w \times \vec{B}_{\text{wave}}$) is smaller than v_z . This results in a decreasing $\gamma_{||}$. The magnetic component of the wave converts $\gamma_{||}$ into transverse energy to be dissipated by the \tilde{E}_\perp . The time evolution of γ , $\gamma_{||}$, and γ_\perp evaluated at $z=L$ and averaged over wiggler periodic is displayed in Fig. 5. The result clearly shows that both $\gamma_{||}$ and γ_\perp are reduced after the peniotron interaction. The nonlinear saturation mechanism may come from the fact that as a result of the interaction v_z is decreased to such an extent that the second harmonic wiggler beam line can no longer couple to the TE₃₁ mode. At the same time, the drift of the center of the helical motion induces higher harmonic contents in electron helical motion which could contaminate the desired peniotron interaction.

In order to determine the bandwidth of the proposed amplifier, the input frequency was varied from $\omega_0=1.1\omega_c$ to $1.6\omega_c$ and the input power was adjusted to optimize the output efficiency. The linear gain and nonlinear efficiency determined from simulation results are shown in Fig. 6a. The bandwidth estimated from these results is more than 30%. The effects of beam current on the performance of the amplifier is displayed in Fig. 6b. The results show that $I=80A$ is the optimal beam current for maximizing the efficiency and gain. Using an initial 1% axial velocity spread or a 3% guiding center spread only reduces the efficiency by 3%.

IV. Summary

In summary, we have investigated the performance of helical peniotron amplifiers and concentrated on demonstrating the physical mechanism. No attempt has been made to optimize the design parameters. The potential advantages of this

configuration are that it converts both beam longitudinal and transverse energy into coherent radiation, its bandwidth is rather wide, and its helical beam structure reduces the severity of mode competition.

ACKNOWLEDGEMENT

This work was supported by the DoD MURI Program (High Energy Microwave Source) as managed by AFOSR under Grant No. F49620-95-1-0253, the Tri-Services initiatives under Grant No. F49620-94-1-0426, and the San Diego Supercomputing Center.

Table I. Second Harmonic Helical Peniotron Amplifier

| | |
|--------------------------------------|------------|
| Beam Voltage | 215 kV |
| Beam Current | 80 A |
| Mode | π mode |
| Number of Vanes | 6 |
| $\alpha = v_{\perp} / v_{\parallel}$ | 0.45 |
| Interaction Length (L) | 24 cm |
| $\omega_c / 2\pi$ | 25 GHz |
| Inner Circuit Radius (a) | 0.16 cm |
| Outer Circuit Radius (b) | 0.304 cm |
| Guide Field (B_0) | 8 kG |
| Wiggler Field (B_w) | 1.1 kG |
| Wiggler Period (λ_w) | 2 cm |

REFERENCES

1. D. B. McDermott, D. S. Furno, and N. C. Luhmann, J. Appl. Physics, 58, 4501(1985).
2. G. P. Scheitrum, R. S. Symons, and R. B. True, Technical digest of IEDM, 743, 1989.
3. P. S. Rha, L. R. Barnett, J. M. Baird, and R. W. Gnow, IEEE Trans. on Electron Devices, 36, 789(1989).
4. K. Yokoo, and H. Shimawaki, H. Tadano, T. Ishihara, K. Sagae, N. Sato, and S. Ono, in 17th Int. Conf. Infared and Millimeter Waves, P. 498 (1992).
5. A. K. Ganguly, G. S. Park, and C. M. Armstrong, IEEE Trans. on Plasma Science, 22, 902(1994).
6. J. M. Baird, Gyrottron Theory in High Power Microwave Sources, V. L. Granatstein and I. Alexeff eds, p. 103(1987, Artech House).
7. A. T. Lin and C.-C. Lin, IEEE Trans. on Plasma Science, 22, 889(1994).
8. A. T. Lin and C.-C. Lin, to appear in Appl. Physics Letters (1995).
9. G. Dohler and D. Gallagher, Int. J. Electronics, 64, 483(1988).
10. K. R. Chu and A. T. Lin, Phys. Rev. Letters, 67, 3235(1991).
11. N. M. Kroll and E. L. Willis, J. Appl. Phys, 19, 166(1947).
12. T. H. Kho and A. T. Lin, Nuclear Instruments and Methods in Phys. Research, A296, 642(1990).

Figure Captions:

- Figure 1 Electron trajectories in a combined solenoidal and wiggler magnetic field: (a) three dimensional spatial trajectory and (b) end view of v_y versus v_z .
- Figure 2 Six vane slotted waveguide and an axis encircling beam: (a) cross-sectional view (the dots are schematic representation of beam electrons) and (b) dispersion curves.
- Figure 3 Performance of a helical peniotron amplifier: (a) spatial distribution of the injected wave power and (b) electron kinetic energy versus axial distance.
- Figure 4 Test electron behavior as it travels through the interaction region: (a) electron-wave coupling and (b) electron transverse trajectory.
- Figure 5 Time evolution of beam energy at $z=L$: (a) total energy, (b) longitudinal energy, and (c) transverse energy.
- Figure 6 Gain and efficiency versus: (a) input frequency ($I=80A$) and (b) beam current ($\omega_0=1.2\omega_c$).

(a)

